




Article

Effect of Microchemistry Elements in Relation of Laser Welding Parameters on the Morphology 304 Stainless Steel Welds Using Response Surface Methodology

Kamel Touileb ^{1,*}, Elawady Attia ², Rachid Djoudjou ¹, Abdejlil Chihoui Hedhibi ³, Abdallah Benselama ⁴, Albaijan Ibrahim ¹ and Mohamed M. Z. Ahmed ^{1,5}

¹ Department of Mechanical Engineering, College of Engineering in Al-Kharj, Prince Sattam bin Abdulaziz University, P.O. Box 655, Al-Kharj 16273, Saudi Arabia; r.djoudjou@psau.edu.sa (R.D.); i.albaijan@psau.edu.sa (A.I.); moh.ahmed@psau.edu.sa (M.M.Z.A.)

² Department of Industrial Engineering, College of Engineering in Al-Kharj, Prince Sattam bin Abdulaziz University, P.O. Box 655, Al-Kharj 16273, Saudi Arabia; e.attia@psau.edu.sa

³ Laboratory of Mechanics of Sousse (LMS), National Engineering School of Sousse, University of Sousse, BP 264, Erriaydh City, Sousse 4023, Tunisia; abdejliloueslati@yahoo.fr

⁴ Department of Electrical Engineering, College of Engineering in Al-Kharj, Prince Sattam Bin Abdulaziz University, P.O. Box 655, Al-Kharj 16273, Saudi Arabia; a.benselama@psau.edu.sa

⁵ Department of Metallurgical and Materials Engineering, Faculty of Petroleum and Mining Engineering, Suez University, Suez 43512, Egypt

* Correspondence: k.touileb@psau.edu.sa



Citation: Touileb, K.; Attia, E.; Djoudjou, R.; Hedhibi, A.C.; Benselama, A.; Ibrahim, A.; Ahmed, M.M.Z. Effect of Microchemistry Elements in Relation of Laser Welding Parameters on the Morphology 304 Stainless Steel Welds Using Response Surface Methodology. *Crystals* **2023**, *13*, 1138. <https://doi.org/10.3390/cryst13071138>

Academic Editors: Reza Beygi, Mahmoud Moradi and Ali Khalfallah

Received: 28 June 2023
Revised: 13 July 2023
Accepted: 18 July 2023
Published: 21 July 2023



Copyright: © 2023 by the authors. Licensee MDPI, Basel, Switzerland. This article is an open access article distributed under the terms and conditions of the Creative Commons Attribution (CC BY) license (<https://creativecommons.org/licenses/by/4.0/>).

Abstract: Small differences in the contents of surface active elements can change flow direction and thus heat transfer, even for different batches of a given alloy. This study aims to determine the effects of sulfur on weld bead morphology in the laser process. The paper presents the results related to the weld bead shape of two thin AISI 304 industrial stainless steel casts. One cast contains 80 ppm (0.008%) of sulfur, considered as a high sulfur content, and the other one contains 30 ppm (0.003%) sulfur, which can be considered low sulfur. The welds were executed using a CO₂ laser. The effects of laser power (3.75, 3.67, 6 kW), welding speed (1.25, 2.40, 2.45, 3.6 m/min), focus point position (2, 7, 12 mm), and shield gas (Helium, mixed 40% helium + 60% argon and mixed 70% helium + 30% argon) with a flow rate of 10 L/min on the depth of the weld (D) and the aspect ratio ($R = D/W$) were investigated using RSM (response surface methodology). The experimental results show that the transfer of energy from the laser beam to the workpiece can be total in cases where the selected welding parameters prevent plasma formation. For the 304 HS cast, the focus point is the major factor in determining the depth of penetration, and its contribution is up to 52.35%. However, for 304 LS, the interaction between shield gas and focus point seems to play an important role, and the contribution of their interaction raises to 28% in relation to the laser depth of the weld. Moreover, the study shows that sulfur plays a surface-active role only in the case of partial penetration beads, so that a 56% partially penetrated weld supports the hypothesis of its surface-active role in the formation of the weld pool. However, a penetration of only 36% confirms the effects of a sulfur surface-active when the bead is fully penetrated.

Keywords: laser welding; AISI 304 SS casts; surfactant elements; marangoni convection; RSM

1. Introduction

Nowadays, laser welding is widely used in many industries, such as in automobiles, aircraft, marines, shipbuilding and aviation. Laser welding is used in modern industry, and has many advantages such as less distortion, greater deep weld bead, and narrow welds compared to traditional welding technologies. As the beam can be concentrated in a small area, it provides a concentrated heat source, leading to narrow and highly penetrated welds [1,2]. Laser welding can be performed without filler materials and single-pass

laser procedures have been employed in materials of up to 32 mm thick. This technique is strongly recommended for use on welding zones requiring high precision and high quality. The laser can be readily mechanized for automated, high-speed welding. Laser welding is a technique that meets the requirements of modern manufacturing in terms of the repeatability of the process and its easy automation. The lasers predominantly used in industrial material processing and welding tasks are the 1.0 μm YAG laser and the 10.6 μm CO₂ laser, with the most common active elements employed in these two types of lasers being neodymium (Nd) ion and CO₂ molecule, respectively [3]. Laser welding processes are classified as focused heat source or high-intensity and high-energy beams. Laser beam welding is one of the most promising welding techniques owing to the higher welding speeds it offers, and the lower dimensions and distortions in the welds. Moreover, its high strength-to-weld geometries and minimal heat-affected zones make it advantageous for various industrial applications. Lasers are characterized by requiring less time, which implies a lower labor cost.

The most commonly used casts of stainless alloys are austenitic steels, known as 8–18 types, which contain 16 to 18% Cr, 6–8% N and 0.03–0.1% C. Austenitic stainless steels are widely used for different applications in the chemical, petrochemical, food processing and nuclear industries, given their good mechanical and plastic properties. Austenitic stainless steels are widely used in a variety of applications owing to their corrosion resistance, good ductility, toughness, and ease of manufacture. The 300 series alloys designated by the American Iron and Steel Institute (AISI) are the most widely used of the austenitic casts. Stainless steels can generally be welded with all methods of fusion welding and solid-state welding [4,5].

The soundness of the weld is intimately related to multiple input parameters. The mastering of these inputs leads to welds with fewer defects. Finding out the optimal combinations is the main target in any research study, and finding the effective combinations is essential [6]. The optimization of welding conditions is useful in order to achieve good properties in the joints. Many researchers have applied various optimization methods to define the desired output variables, by developing mathematical models to specify the relationship between depth and welding parameters. Sampreeta et al. [7] examined bead-on-plate welding on Hastelloy C-276 plates of 1.6 mm thickness using the CO₂ laser welding process. The welding was performed based on the Taguchi L9 design, considering laser power, welding speed and the flow rate of the shielding gas as input parameters. They found that a laser power of 1600 W, welding speed of 2 m/min and shielding gas flow rate of 10 L/min gave the best results. Using analysis of variance (ANOVA), it was found that laser power is the most influential parameter on the quality of the welds.

Another study conducted by Sathiya et al. [8] was dedicated to the optimization of laser bead-on-plate welding parameters with a 3.5 kW laser using Taguchi technique. The experiments were conducted on two different shielding gases: 100% nitrogen and a gas mixture of 50% nitrogen and 50% argon. The most suitable input process parameters, such as beam power, travel speed and focus position, were selected in order to obtain the desired output, i.e., bead width and depth of penetration. They concluded that beam power (42.35%) has a greater influence on welding, followed by focus position (27.48%) and travel speed (19.07%), when 100% nitrogen shielding gas is used. However, when a mixed gas (50% N, 50% Ar) was tested, they found that the travel speed (35.06%) has more influence on the welding, followed by focus position (29.71%) and beam power (28.81%). Anawa et al. [9] successfully applied a CO₂ laser welding process and optimized the process parameters for joining dissimilar AISI 316 stainless steel and AISI 1009 low carbon steel plates. RSM was used to develop the mathematical models employed to predict the heat input and to describe the laser weld bead profile for a continuous wave 1.5 kW CO₂ laser. In their study, the laser input parameters, such as laser power, welding speed and focused position, were taken into consideration. Benyounis et al. [10] conducted a study to optimize autogenous laser welded joints to get the maximum penetration, and the minimum fusion zone width and heat-affected zone width. In order to achieve these objectives, the authors

developed a mathematical model and optimized the weld bead profiles. Several studies have confirmed the preponderant role played by surface active elements such as Se, Te, O, and S in the determination of the weld bead [11,12]. These studies, most of which were carried out in TIG (tungsten inert gas), show that a sulfur-rich cast presents a narrow and deep weld appearance. Contrarily, a cast free of sulfur presents a wide and more shallow bead [13]. In spite of the large amount of literature available on the effects of surfactant elements on TIG welding, very little work has been reported so far on the effects of the above-mentioned element during laser welding. Zhao et al. [14] were interested in the effects of adding oxygen as a surfactant on convection molten metal. Stainless steel samples were subjected to laser spot welding in an environmentally controlled chamber in order to observe fluid flow behavior and examine the influence of oxygen concentration on the flow. Transitions in fluid flow direction were observed during laser spot welding, whereby an initial outward flow changed to an inward flow in the presence of an oxidizing atmosphere. This behavior can be explained in terms of changes in surface tension gradients driven by oxygen dissolution in the liquid metal. Flow reversal only occurs in the presence of sufficient environmental oxygen. CO₂ lasers are still the predominant type of laser used in the manufacturing industry, and in the higher power ranges in particular. Conduction mode welding occurs when heat is transferred from the surface into the material via thermal conduction. Conduction welding is made possible when the absorbed energy is sufficient to melt the weld zone, but insufficient for vaporization and plasma formation [15,16]. On the other hand, keyhole welding represents a type of welding wherein the laser beam energy is transferred deep into the material through a cavity filled with ionized metal vapor.

In simulations of heat conduction laser welding, the effect of the temperature-dependent surface tension coefficient (Marangoni effect) was identified as the primary driving force of the liquid melt. This coefficient is the most important driving force of the melt in conventional welding. In this study, the simulations show large differences in flow behavior caused merely by inverting the temperature dependency of $\gamma(T)$. Therefore, the Marangoni effect is very important in deep laser welding. The simulations confirm and clarify the observed variations in weld bead geometry that arise due to very different flow patterns. These differences result from the marginal fluctuations in the chemical composition within the tolerance of the standard defining the material composition of a special alloy [17]. C. R. Heiple et al. [18] confirmed that the addition of small concentrations of a surface active element (Se) to stainless steel dramatically increased the D/W ratio of a severely defocused and decoupled laser weld. A defocused laser weld strongly supports the surface tension-driven fluid flow model.

Kaul et al. [19] studied the effects of the active flux laser beam welding of austenitic stainless steel sheets on plasma plume. Laser welding using SiO₂ flux significantly modified the shape of the fusion zone (FZ), which produced narrower and deeper welds. The development of such a weld bead is caused by a reversal in the direction of the Marangoni flow caused by the oxygen-induced inversion of surface tension gradient. Ding et al. [20] reported that both the surface-activating flux and surface active element S produce significant effects on the YAG laser weld shape in terms of increased weld penetration and depth/width ratio. Su et al. [21] reported that the CO₂ LBW (laser beam welding) of AISI 304 stainless steel sheets with active flux resulted in an increased weld depth through a decrease in the electron density of the plasma plume. In contrast, active flux had little effect on the depth of Nd:YAG laser welds [22]. The direction of the convective (or Marangoni) flow in the weld pool is governed by the sign of the surface tension gradient dy/dT .

The research focuses on weldability problems related to the cast-to-cast variation in the weld pool geometry and penetration between materials with almost the same chemical compositions. The aim of our study is to analyze the influence of the basic parameters of laser welding (i.e., laser beam power, welding speed, shield gas types and focal point position) on the weld shape. This study is conducted on two industrial casts comprising AISI 304 austenitic stainless steel sheets of 3.0 mm thickness. The RSM optimization method is used to develop a mathematical model of depth and aspect ratio in terms of

welding parameters. The optimal surface design in terms of response is used to design the experiment. The model required 15 points, and another 15 points were added randomly to increase the model efficiency using Design Expert Software. After performing the multi-regression analysis using Design Expert software, equations were obtained.

The laser welding parameter plays an important role in the quality of the weld, and hence the quality of the joint produced in industry. These results reveal the welding conditions that allow the surface active elements to play their fullest role. Furthermore, the results obtained in this study offer interesting data for researchers to relate the heat applied (welding parameters) with heat the weld profile, and the ensuing changes in microstructure. The microstructural properties are strongly affected by heat transfer and metal flow in the weld pool.

2. Materials and Methods

2.1. Materials

Two casts of austenitic stainless steel, AISI 304 LS and AISI 304 HS, with thicknesses of 3 mm were investigated in this study. The chemical compositions are presented in Table 1.

Table 1. Chemical composition (wt. %) of 304 stainless steel casts.

Elements	C	Mn	Si	P	S	Cr	Ni	Fe
304HS SS	0.06	0.86	0.41	0.024	0.008	18.29	8.40	Balance
304LS SS	0.06	1.06	0.57	0.032	0.003	18.29	8.45	Balance

The sulfur content, thermal gradient and surface tension at melting temperature of the casts used are given in Table 2. Figure 1 shows the evolution of surface tension versus the temperature for both casts.

Table 2. Surface tension at melting temperature, thermal gradient and sulfur content of used casts [23].

Elements	γ (N/m) at Melting Temperature	$d\gamma/dT$ (N/m °K)	Sulfur Content (%)
304HS SS	1.62	$+8 \times 10^{-5}$	0.008
304LS SS	1.74	-10^{-5}	0.003

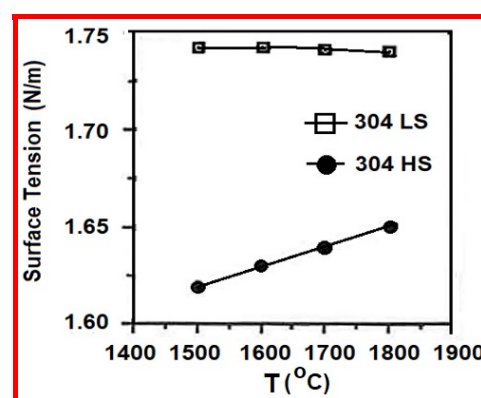


Figure 1. Surface tension against temperature of 304 SS casts [23].

The surface tension of the liquid metal is dependent upon its temperature, and therefore dependent upon the distance from the center of the weld pool, since a molten weld pool has a radial temperature gradient such that the highest temperature is directly beneath the source of heat, and the lowest is at the solid–liquid interface. The combination of the dependence of the surface tension (γ) on the temperature (T) and the presence of a temperature gradient causes a surface tension gradient ($d\gamma/dT$) even in a small region.

Figure 1 represents the variation in surface tension against temperature in the center of the weld pool. In molten metal, in the case of a 304 LS cast, a decrease in the surface tension as the temperature increases is ascribed to the absence or quasi-absence of surfactants (30 ppm of Sulfur). In the case of 304 LS, the slope is negative (the temperature coefficient of the surface tension is negative).

However, in 304 HS (with 80 ppm), by contrast, the surface tension is highest at the center. As the melting point is reached, the molten metal flows from the center to the edge. Sulfur is a strongly surface-active element that segregates in the surface layer and reduces surface tension. However, as the temperature increases, sulfur desorbs into the bulk of the liquid metal, causing an increase in surface tension. This applies to alloys with a sulfur content greater than 50 ppm [24,25]. The surface tension will be highest at the center and thus the surface flow will be radially inward, and this will induce a downward flow in the center, called inverse Marangoni convection. In the case of 304 HS, the slope is positive (positive temperature coefficient of surface tension). A shallow, wide weld bead can be obtained in low-sulfur (S) stainless steel (30 ppm); however, a deep, narrow penetration weld is obtained in the case of a sulfur (S) content of 80 ppm.

2.2. Welding Procedure

The welding tests were carried out using the laser installation of the central school of Nantes (France), with a carbon dioxide (CO_2) laser capable of producing a maximum output of 6 kW and emitting radiation in the infrared band of $10.6 \mu\text{m}$ and a pressure of 100 Pa. The laser gas was composed of $\text{He} + \text{N}_2 + \text{CO}_2$. Figure 2a depicts the CO_2 laser welding modes, and Figure 2b shows laser beam welding in progress, with a shiny dazzling light.

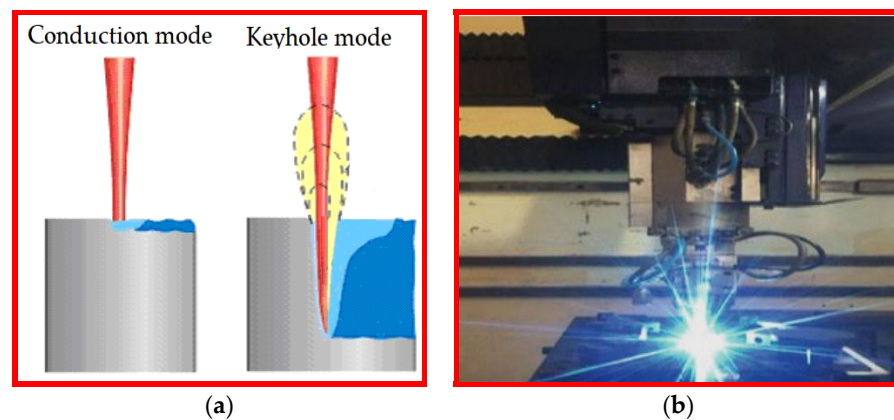


Figure 2. (a) Laser welding modes [26], (b) laser beam welding in progress [27].

Table 3 depicts the physical properties of the shield gas used. A preliminary study of the welding parameters is necessary to adjust the specific energy supplied to the sheets. The experiments involved welding a 120 mm line on a rectangular plate of 3 mm thickness, 150 mm length and 80 mm width. Before welding, the plates were cleaned with acetone.

Table 3. Physical properties of shield gas used.

Laser Welding Gas	Molecular Weight (g/mol)	Thermal Conductivity at 1 bar, 15 °C (W/m·K)	Ionization Energy (ev)	Dissociation Energy (ev)	Density Relative to Air
Helium	4	0.15363	24.6	0	0.14
Argon	40	0.01732	15.8	0	1.38

In this study, 30 tests were carried out on each cast. Four factors were considered at different levels, as presented in Table 4. Three focus lengths were tested (+2, +7, +12 mm). Four welding speeds were investigated (1.25, 2.40, 2.45, 3.6 m/min). Three levels of power were applied (3.75, 3.67, 6 kW). In addition, three levels of the shield gas were considered according to the proportion of helium (40% helium mixed with 60% of argon, 70% helium mixed with 30% argon, and 100% helium). Figure 3 depicts the focus point positions used during the CO₂ laser beam welding experiments.

Table 4. Laser welding parameters.

Runs	Focus Point Position (mm)	Welding Speed (m/min)	Power (kW)	Linear Energy (J/cm)	Shield Gas
1	2.00	1.25	3.75	180	1 (70% He + 30% Ar)
2	2.00	2.45	3.67	90	1 (70% He + 30% Ar)
3	2.00	2.40	6.00	150	1 (70% He + 30% Ar)
4	2.00	3.60	6.00	100	1 (70% He + 30% Ar)
5	7.00	1.25	3.75	180	1 (70% He + 30% Ar)
6	7.00	2.40	6.00	150	1 (70% He + 30% Ar)
7	2.00	1.25	3.75	180	2 (100% He)
8	2.00	2.45	3.67	90	2 (100% He)
9	2.00	2.40	6.00	150	2 (100% He)
10	2.00	3.60	6.00	100	2 (100% He)
11	2.00	1.25	3.75	180	3 (40% He + 60% Ar)
12	2.00	2.45	3.67	90	3 (40% He + 60% Ar)
13	2.00	3.60	6.00	100	3 (40% He + 60% Ar)
14	2.00	2.40	6.00	150	3 (40% He + 60% Ar)
15	12.00	1.25	3.75	180	2 (100% He)
16	12.00	2.45	3.67	90	2 (100% He)
17	12.00	2.40	6.00	150	2 (100% He)
18	12.00	3.60	6.00	100	2 (100% He)
19	7.00	2.40	6.00	150	3 (40% He + 60% Ar)
20	7.00	2.40	6.00	150	2 (100% He)
21	12.00	1.25	3.75	180	3 (40% He + 60% Ar)
22	12.00	2.45	3.67	90	3 (40% He + 60% Ar)
23	12.00	2.40	6.00	150	3 (40% He + 60% Ar)
24	12.00	3.60	6.00	100	3 (40% He + 60% Ar)
25	7.00	2.45	3.67	90	1 (70% He + 30% Ar)
26	7.00	2.40	6.00	150	1 (70% He + 30% Ar)
27	12.00	1.25	3.75	180	1 (70% He + 30% Ar)
28	12.00	2.45	3.67	90	1 (70% He + 30% Ar)
29	12.00	2.40	6.00	150	1 (70% He + 30% Ar)
30	12.00	3.60	6.00	100	1 (70% He + 30% Ar)

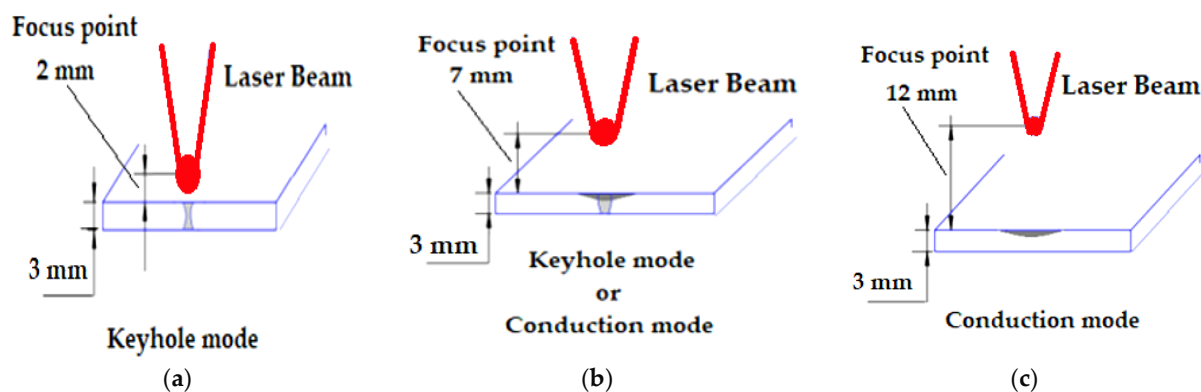


Figure 3. Scheme of the CO₂ laser beam focus positions used: (a) focus point = 2 mm, (b) focus point = 7 mm, (c) focus point = 12 mm.

The surface design yielding the optimal response has been used to design this experiment. The model required 15 points, and another 15 points were added randomly to increase the model efficiency using Design Expert software. First, a series of trials were conducted to master the welding parameters that were to be selected for our tests. In each test, three coupons were cut from the welding line to ensure the reproducibility and reliability of the results obtained. The samples were prepared by grinding, and subsequently polished, with a diamond suspension of 6 μm and 1 μm , respectively, then etched by immersion in Carpenters solution (8.5 gm FeCl_3 , 2.4 gm CuCl_2 , 122 mL alcohol, 122 mL HCl , 6 mL HNO_3) for macrographic analysis. The samples were observed and checked using Motic software integrated with an optical microscope. The results of the weld aspect (depth of penetration, weld width) represent an average of the three readings.

2.3. Mathematical Modeling

Using regression analysis, a mathematical model can be obtained that relates the output responses to the function of the input parameters. After the preliminary investigation, a mathematical formulation can be formed using the cubic polynomial relation. The cubic or third order polynomial function can be expressed as represented in Equation (1).

$$Y = b_0 + \sum_{i=1}^n b_i X_i + \sum_{j>i}^n b_{ij} X_i X_j + \sum_{i=1}^n b_{ii} X_i^2 + \sum_{k>j>i}^n b_{ijk} X_i X_j X_k + \sum_{j>i}^n b_{ij} X_i X_j^2 + \sum_{i=1}^n b_{iii} X_i^3 + \varepsilon \quad (1)$$

where X_i represents the four input factors, such that $i \in \{f, s, p, g\}$; b represents the coefficient corresponding to the specified terms; b_0 is the constant term, b_i is the coefficient of the linear terms; b_{ij} is the coefficient of the linear interaction terms and b_{ijk} is the coefficient of the interaction terms among the linear and quadratic order; b_{iii} is the coefficient of the cubic terms. We used Design Expert software, with the cubic model and auto selection of terms relying on the adjusted R^2 .

3. Results and Discussion

3.1. 304 HS Stainless Steel Cast

Figure 4 represents the micrographs of the laser welding of high-sulfur content casts, carried out with a power of 6 kW, a welding speed of 2.4 $\text{m}\cdot\text{min}^{-1}$, and a shield gas comprising 70% He + 30% Ar. It shows a keyhole weld bead with a focus distance of 2 mm and 7 mm. However, we see that the weld is partially penetrated when the focus point is 12 mm away from the workpiece.

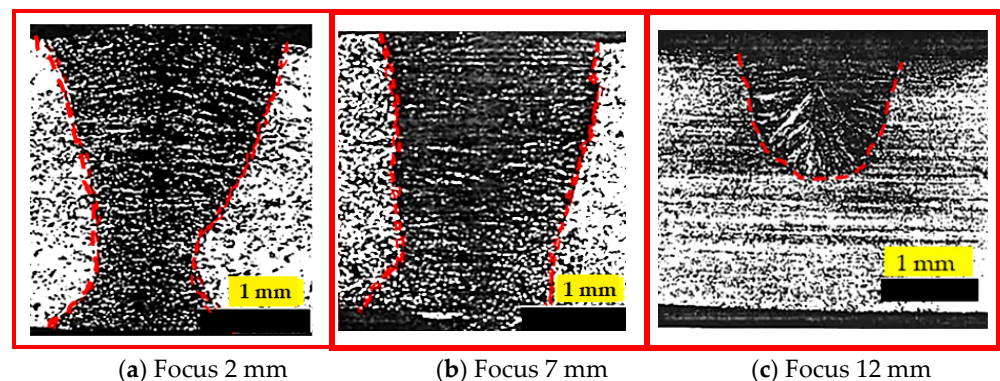


Figure 4. Effect of focus point on 304 HS laser weld carried out with a power 6 kw, welding speed 2.4 $\text{m}\cdot\text{min}^{-1}$, and shield gas comprising 70% He + 30% Ar.

The effects of the laser welding parameters on the welds' morphology are gathered in Table 5, where the input (investigated) factors and responses are presented.

Table 5. Investigated factors and the responses for 304 HS.

Runs	Investigated Factors				Response Variables	
	X _f (Focus Point) (mm)	X _s (Weld Speed) (m/min)	X _p (Power) (kW)	X _g (Shield Gas Type)	Y _d Depth (mm)	Y _r R (D/W)
1	2	1.25	3.75	1 (70% He + 30% Ar)	3	1.6
2	2	2.45	3.674	1 (70% He + 30% Ar)	3	1.8
3	2	2.4	6	1 (70% He + 30% Ar)	3	1.42
4	2	3.6	6.001	1 (70% He + 30% Ar)	3	1.75
5	7	1.25	3.75	1 (70% He + 30% Ar)	3	1.17
6	7	2.4	6	1 (70% He + 30% Ar)	3	1.36
7	2	1.25	3.75	2 (100% He)	3	1.41
8	2	2.45	3.674	2 (100% He)	3	2.1
9	2	2.4	6	2 (100% He)	3	2.1
10	2	3.6	6.001	2 (100% He)	3	2.14
11	2	1.25	3.75	3 (40% He + 60% Ar)	3	1.14
12	2	2.45	3.674	3 (40% He + 60% Ar)	3	1.71
13	2	2.4	6.00	3 (40% He + 60% Ar)	3	1.76
14	2	3.6	6.001	3 (40% He + 60% Ar)	3	2.17
15	12	1.25	3.75	2 (100% He)	0.6	0.29
16	12	2.45	3.674	2 (100% He)	0.41	0.26
17	12	2.4	6.00	2 (100% He)	1.40	0.77
18	12	3.6	6.001	2 (100% He)	0.55	0.31
19	7	2.4	6.00	3 (40% He + 60% Ar)	2.01	0.82
20	7	2.4	6.00	2 (100% He)	1.92	0.71
21	12	1.25	3.75	3 (40% He + 60% Ar)	0.7	0.39
22	12	2.45	3.674	3 (40% He + 60% Ar)	0.4	0.28
23	12	2.4	6.00	3 (40% He + 60% Ar)	0.79	0.47
24	12	3.6	6.001	3 (40% He + 60% Ar)	0.41	0.23
25	7	2.45	3.674	1 (70% He + 30% Ar)	1.64	0.77
26	7	3.6	6.001	1 (70% He + 30% Ar)	1.96	0.73
27	12	1.25	3.75	1 (70% He + 30% Ar)	0.5	0.25
28	12	2.45	3.674	1 (70% He + 30% Ar)	0.48	0.31
29	12	2.4	6.00	1 (70% He + 30% Ar)	1.77	0.61
30	12	3.6	6.001	1 (70% He + 30% Ar)	1.91	1.08

Based on the results depicted in Table 5, the first 14 experiments gave full penetrated welds. All the cited runs were executed with different welding speeds and powers, but with a constant focus point of 2 mm. In this case, keyhole mode heat transfer occurred. A high-energy density laser beam vaporizes the workpiece during the welding process to form a hole, which allows the laser beam to penetrate into the metal to produce a deep, narrow melt pool, thus leading to a high aspect ratio. The range of values of the weld aspect ratio is between 1.14 and 2.17. The combination of a high ionization energy and the high thermal conductivity of helium favors higher weld aspects in comparison to mixing gas (He, Ar). Once the laser beam is defocussed at focus point 7 mm or 12 mm from the

workpiece, the weld becomes partially penetrated, despite the high content of sulfur in the cast 304 HS. The effect of sulfur as a surfactant element is hidden and not obvious.

At a high energy level, helium as well as mixed gas (70% He + 30% Ar) produces larger weld beads than those produced under the shield gas mixture (40% He + 60% Ar). This is attributed to the fact that helium is characterized by a high ionization potential, which provides better protection of the weld pool by expelling the plasma and ensuring less heat loss transfer. On the other hand, at high linear energy and under a gas mixture with 60% argon, there is a risk of argon ionization, which causes the formation of plasma.

3.1.1. Regression Model for Weld Depth (Y_d)

After performing the multi-regression analysis using Design Expert software, excluding two outliers, the mathematical model shown in Equation (2) can be obtained for the responses variable Y_d .

$$Y_d = 7.03481 + 0.10019 X_f + 0.85970 X_s - 1.18023 X_p - 13.46056 X_g - 0.49642 X_f X_s + 0.19418 X_f X_p + 0.52264 X_f X_g + 2.55656 X_p X_g - 0.04246 X_f^2 + 9.12357 X_g^2 + 0.03329 X_f^2 X_s - 0.01132 X_f^2 X_p - 0.35694 X_f X_g^2 - 1.73172 X_p X_g^2 \quad (2)$$

The statistical indicators specify the significance of the proposed mathematical model. Figure 5 shows (a) the normal plot of residuals and (b) the predicted transformed data as compared to the actual transformed data. The normal plot of residuals depicts that the residuals (errors) are approximately normally distributed. This means the errors are independent and random. Also, this distribution indicates the quality of the regression model. The ANOVA results confirm the statistical significance of the proposed mathematical model, as listed in Table 6. The proposed mathematical model is significant when F-value = 73.46 is sufficiently high. The values of R^2 are as follows: obtained $R^2 = 0.9875$, adjusted $R^2 = 0.9741$, and predicted $R^2 = 0.9438$. The difference between R^2 and the adjusted R^2 is small (less than 0.2), which indicates the statistical significance of the equation. Moreover, the signal-to-noise ratio is sufficiently high, $S/N = 21.417$, which shows the adequacy of the model in representing data that can be used to design high-quality systems.

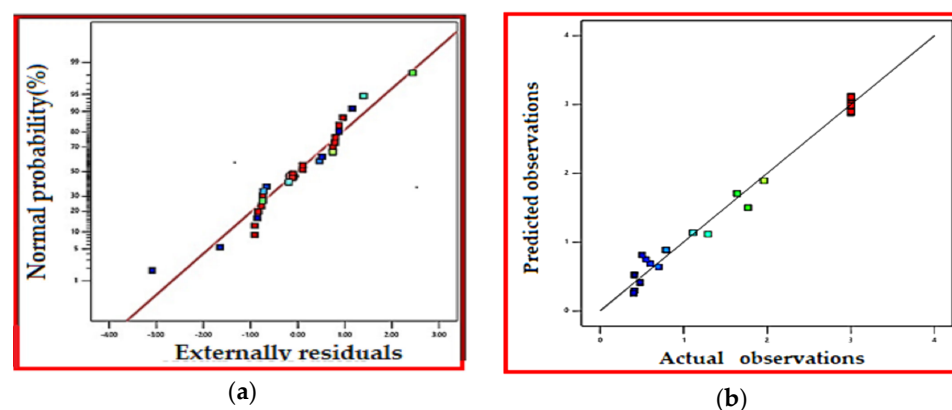


Figure 5. Statistical indicators model. (a) Normal plot of residuals; (b) predicted vs. actual observations for Y_d .

As regards the ANOVA results, the major contributor is the factor focus point (X_f), which contributes about 52.35% of the data variance with a linear effect. The second parameter is welding speed (X_s); its linear effect contributes about 9.04% of the data variance. The third factor is X_p , which shows a percentage of 5.66%. The interaction effect between the quadratic form (X_f) and X_s gives a contribution of about 5.54%. This interaction effect can be seen in Figure 6a, where the contour lines are not linear. The interaction effect between X_f and X_p is significant, with a contribution of 3.39%, as shown in Figure 6b, where the contour lines seem to be linear. Many other terms are significant; however, their contributions are small. For example, the quadratic form of X_f^2 shows 2.84%,

and the interaction form ($X_f X_s$) shows 1.29%. Some terms give a contribution of about 1%, for example, ($X_p X_g^2$), ($X_f^2 X_p$), ($X_f X_g^2$), and (X_g^2). In this model, there are five terms with p -value > 0.05 , which indicates the statistical insignificance of these terms, which are ($X_p X_g$), ($X_f X_g$), (X_g^2), ($X_f X_g^2$) and (X_g). However, these terms were kept in the equation to conserve the hierarchical relation of the model, with very small coefficients.

Table 6. ANOVA results of the Y_d in function of X_f , X_s , X_p and X_g .

Source	Sum of Squares	DF	Mean Square	F-Value	p-Value	Contribution (%)
Model	34.37	14	2.46	73.46	<0.0001	
X_f	8.34	1	8.34	249.44	<0.0001	52.35
X_s	1.44	1	1.44	43.06	<0.0001	9.04
X_p	0.901	1	0.901	26.96	0.0002	5.66
X_g	0.0181	1	0.0181	0.5414	0.4749	0.11
$X_f X_s$	0.2058	1	0.2058	6.16	0.0275	1.29
$X_f X_p$	0.5393	1	0.5393	16.14	0.0015	3.39
$X_f X_g$	0.0189	1	0.0189	0.5658	0.4654	0.12
$X_p X_g$	0.0329	1	0.0329	0.9857	0.3389	0.21
X_f^2	0.4529	1	0.4529	13.55	0.0028	2.84
X_g^2	0.1326	1	0.1326	3.97	0.0678	0.83
$X_f^2 X_s$	0.8819	1	0.8819	26.39	0.0002	5.54
$X_f^2 X_p$	0.1676	1	0.1676	5.02	0.0432	1.05
$X_f X_g^2$	0.1376	1	0.1376	4.12	0.0634	0.86
$X_p X_g^2$	0.1697	1	0.1697	5.08	0.0421	1.07
Residual	0.4344	13	0.0334			
Cor Total	34.8	27	15.9317			

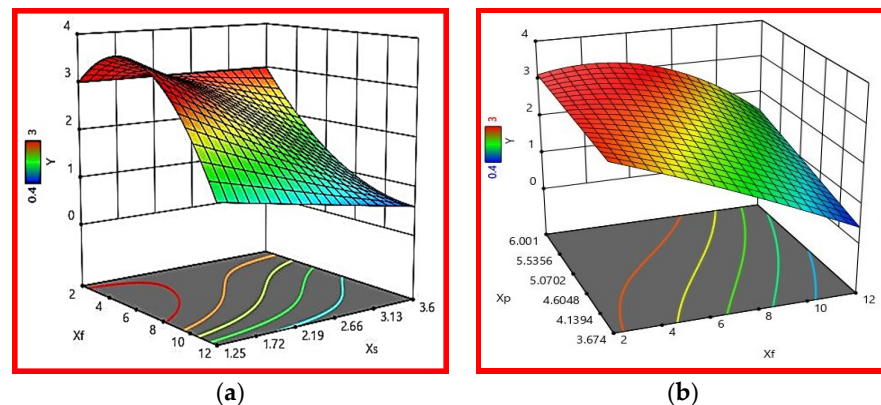


Figure 6. The interaction relationships between (a) X_f and X_s and (b) X_f and X_p for Y_d .

3.1.2. Regression Model for Aspect Ratio (Y_r)

With the same methodology, the mathematical formulation of Y_r can be formulated as in Equation (3) after excluding two outlier points.

$$Y_r = 0.08185 - 0.01150 X_f + 1.32215 X_s - 0.06562 X_p + 0.26042 X_g - 0.35371 X_f X_s + 0.14512 X_f X_p - 0.08525 X_s X_p - 0.00748 X_f^2 + 0.02270 X_f^2 X_s - 0.00942 X_f^2 X_p \quad (3)$$

The statistical indicators show the significance of the proposed formulation. As shown in Figure 7a, the residuals are normally distributed. The residuals sit approximately around the line, which indicates that the errors are normally distributed. Moreover, Figure 7b shows a good distribution of the actual data against the predicted data. The ANOVA results for Y_r are listed in Table 7. As shown, the F-value of the model is high—F-value = 43.59—with a p -value < 0.0001 , which indicates the good fit of the proposed equation for modeling the measured data. The obtained $R^2 = 0.9625$, the adjusted $R^2 = 0.9404$, and the predicted

$R^2 = 0.9145$; these good values confirm the statistical significance of the mathematical model. The signal to noise ratio $S/N = 17.725 > 4$, i.e., an adequate signal. The statistics in Figure 8a,b support the statistical significance of the proposed relation for predicting the effects of Y_r on the functions of the four parameters X_f , X_s , X_p , and X_g .

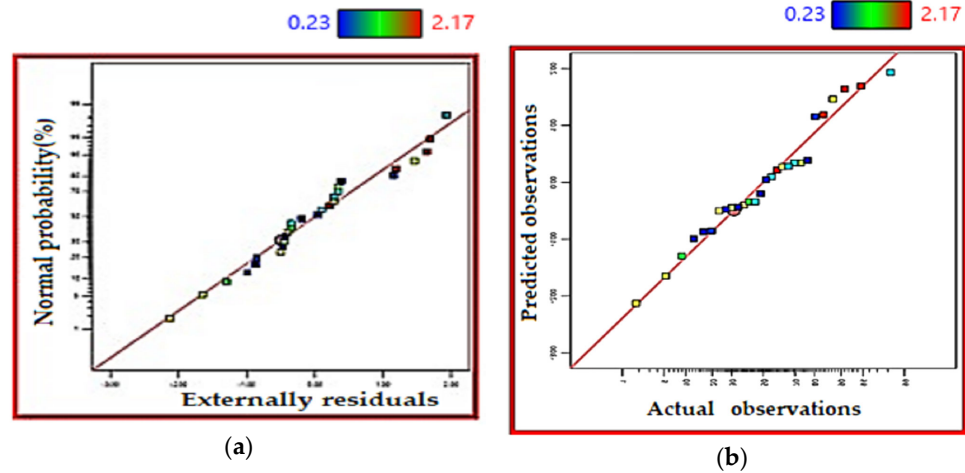


Figure 7. Model statistical indicators. (a) Normal plot of residuals. (b) The predicted vs. actual observations.

Table 7. ANOVA results of the effects of Y_r on the function of X_f , X_s , X_p and X_g .

Source	Sum of Squares	DF	Mean Square	F-Value	p-Value	Contribution (%)
Model	12.86	10	1.29	43.59	<0.0001	
X_f	11.64	1	11.64	394.76	<0.0001	79.76
X_s	0.3061	1	0.3061	10.38	0.005	2.10
X_p	0.2238	1	0.2238	7.59	0.0135	1.53
X_g	0.0977	1	0.0977	3.31	0.0865	0.67
$X_f X_s$	0.2875	1	0.2875	9.75	0.0062	1.97
$X_f X_p$	0.0738	1	0.0738	2.5	0.132	0.51
$X_s X_p$	0.0929	1	0.0929	3.15	0.0939	0.64
X_f^2	0.0085	1	0.0085	0.2886	0.5981	0.06
$X_f^2 X_s$	0.41	1	0.41	13.9	0.0017	2.81
$X_f^2 X_p$	0.134	1	0.134	4.54	0.0479	0.92
Residual	0.5014	17	0.0295			
Cor Total	13.36	27	14.5938			

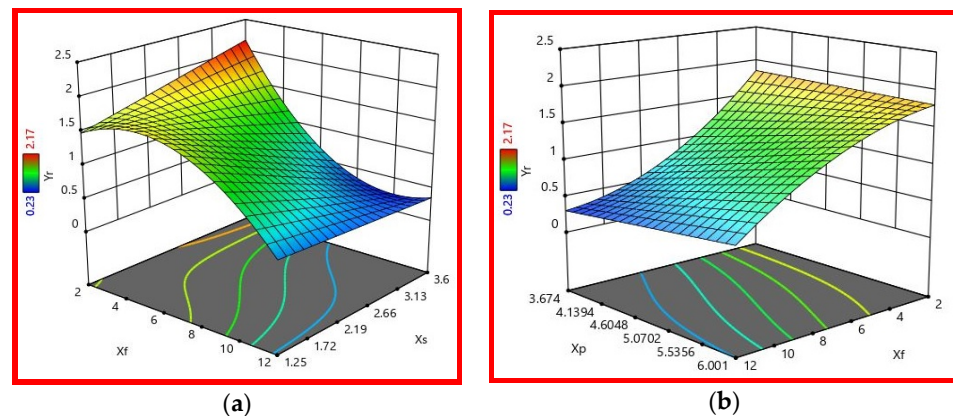


Figure 8. The interaction relationships between (a) X_f and X_s and (b) X_f and X_p for Y_r .

Concerning the different terms of the equation, only ten terms are kept in the equation. The ANOVA results show the statistical significance of the linear terms. The factor X_f is

responsible for the main effect, which contributes about 80% of the variance. The effects of the other variables are small compared to X_f . The second contributor is the third-order term ($X_f^2 X_s$), which contributes with only 2.81%. The interaction relationships between X_f and X_s are shown in Figure 8a. This figure shows that the contour lines are not linear. The other statistically significant terms represent X_s , $X_f X_s$, X_p , and $X_f^2 X_p$, which contribute, respectively, to 2.1%, 1.97%, 1.53%, and 0.92%. As shown in Figure 8b, the interaction relationships between X_f and X_p are weak and nonlinear. There are four insignificant terms that are kept to conserve the hierarchy of the equation, which include X_g , $X_s X_p$, $X_f X_p$, and X_f^2 .

3.2. 304 LS Stainless Steel Cast

Figure 9 shows micrographs of the laser welding of a high-sulfur content cast, carried out with a power of 3.674 kw, a welding speed of $2.450 \text{ m} \cdot \text{min}^{-1}$, and a shield gas comprising 70% He + 30% Ar. It produces a keyhole weld bead with focus distance of 2 mm. However, the weld is partially penetrated when the focus point is 7 mm or 12 mm from the workpiece.

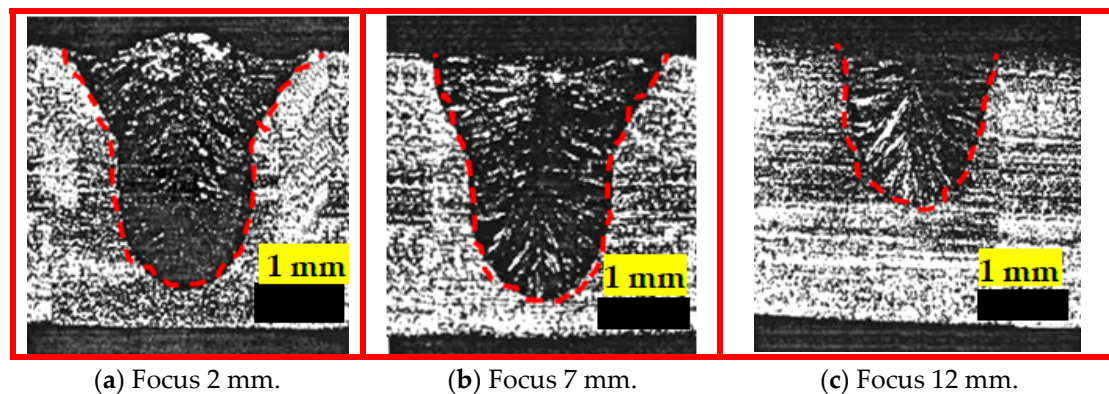


Figure 9. Effect of focus point on 304 LS laser weld carried out with a power of 3.674 kw, a welding of speed $2.450 \text{ m} \cdot \text{min}^{-1}$, and a shield gas comprising 70% He + 30% Ar.

The effects of the laser welding parameters on the welds' morphology are gathered in Table 8, which represents the investigated factors and the responses. We can specifically see that all the welds are partially penetrated. The weld is determined by the thermal conduction mode and surface tension-driven fluid flow in the weld pool. Marangoni convection forces the molten fluid to move from the center to the edges. The welds executed with a 2 mm focus point show greater penetration. Among the 30 experiments, only 7 gave aspect ratio values greater than 1, and the remaining results were all less than 1. These results confirm that the 304 LS welds were wider.

Table 8. Investigated factors and the responses for 304 LS.

Runs	Investigated Factors				Response Variables	
	X_f (Focus Point) (mm)	X_s (Weld Speed) (m/min)	X_p (Power kW)	X_g (Shield Gas Type)	Y_d Depth (mm)	Y_r R(D/W)
1	2	1.25	3.75	1 (70% He + 30% Ar)	1.80	0.84
2	2	2.45	3.674	1 (70% He + 30% Ar)	2.75	1.06
3	2	2.4	6	1 (70% He + 30% Ar)	1.27	0.66
4	2	3.6	6.001	1 (70% He + 30% Ar)	1.26	1.01
5	7	1.25	3.75	1 (70% He + 30% Ar)	1.75	0.64
6	7	2.4	6	1 (70% He + 30% Ar)	1.59	0.70

Table 8. Cont.

Runs	Investigated Factors				Response Variables	
	X _f (Focus Point) (mm)	X _s (Weld Speed) (m/min)	X _p (Power kW)	X _g (Shield Gas Type)	Y _d Depth (mm)	Y _r R(D/W)
7	2	1.25	3.75	2(100% He)	1.60	0.88
8	2	2.45	3.674	2(100% He)	0.80	0.51
9	2	2.4	6	2(100% He)	1.32	0.75
10	2	3.6	6.001	2(100% He)	1.26	1.01
11	2	1.25	3.75	3(40% He + 60% Ar)	1.07	0.61
12	2	2.45	3.674	3(40% He + 60% Ar)	1.12	0.59
13	2	2.4	6.00	3(40% He + 60% Ar)	0.82	0.65
14	2	3.6	6.001	3(40% He + 60% Ar)	1.24	1.02
15	12	1.25	3.75	2(100% He)	0.52	0.24
16	12	2.45	3.674	2(100% He)	0.37	0.22
17	12	2.4	6	2(100% He)	0.77	0.38
18	12	3.6	6.001	2(100% He)	0.39	0.21
19	7	2.4	6.00	3(40% He + 60% Ar)	1.24	0.65
20	7	2.4	6.00	2(100% He)	0.69	0.34
21	12	1.25	3.75	3(40% He + 60% Ar)	0.32	0.16
22	12	2.45	3.674	3(40% He + 60% Ar)	0.90	0.37
23	12	2.4	6	3(40% He + 60% Ar)	0.39	0.18
24	12	3.6	6.001	3(40% He + 60% Ar)	2.62	1.48
25	7	2.45	3.674	1 (70% He + 30% Ar)	2.65	1.20
26	7	3.6	6.001	1 (70% He + 30% Ar)	1.86	0.66
27	12	1.25	3.75	1 (70% He + 30% Ar)	1.53	0.58
28	12	2.45	3.674	1 (70% He + 30% Ar)	1.5	1.07
29	12	2.4	6	1 (70% He + 30% Ar)	1.76	0.66
30	12	3.6	6.001	1 (70% He + 30% Ar)	1.80	0.70

3.2.1. Regression Model for Weld Depth (Y_d)

The weld depth (Y_d) can be modeled as a function of the four parameters using the following equation, after excluding one outlier point:

$$\ln(Y_d) = +1.93616 - 0.598436 X_f - 1.59819 X_s + 0.123277 X_p - 2.16420 X_g + 0.465780 X_f X_s - 0.146866 X_f X_p + 1.93070 X_f X_g + 0.145050 X_s X_p - 0.020255 X_f^2 + 1.74479 X_g^2 - 0.019693 X_f X_s X_p - 0.027802 X_f^2 X_s + 0.015243 X_f^2 X_p - 1.40293 X_f X_g^2 \quad (4)$$

The obtained F-value = 21.51 and *p*-value < 0.0001, which indicates the statistical significant of the mathematical model. There is only a 0.01% chance that an F-value could occur due to noise. Moreover, the obtained value R² = 0.9556, the adjusted value R² = 0.9112, and the S/N = 17.388 indicate a satisfactory fitting of the proposed equation to the data. The accuracy of the mathematical model can be represented by plotting the predicted against the experimental data, as shown in Figure 10b, and by interpreting the normal plot of the residuals shown in Figure 10a. There is a small difference in some points between the experimental and predicted data.

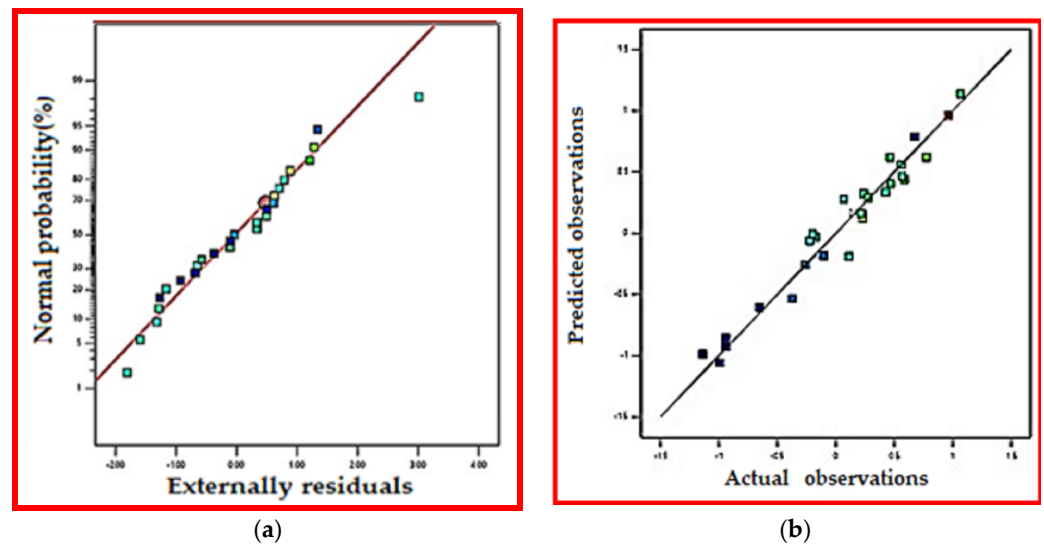


Figure 10. Model statistical indicators. (a) Normal plot of residuals. (b) The predicted observations vs. actual observations.

The ANOVA results are shown in Table 9. They indicate the statistical significance of most of the equation terms. Any term with p -value < 0.05 is considered as statistically significant. One can notice that the interactions between the variables and the higher orders are significant. In this case, x_f , $x_f x_p$, x_f^2 , x_g^2 , $x_f^2 x_s$, $x_f^2 x_p$ and $x_f x_g^2$ are significant model terms. Values greater than 0.1 indicate that the model terms are not significant. Also, the lack of fit is insignificant, as it confirms the statistical significance of the proposed model as regards its ability to express the effect of the four parameters on the depth.

Table 9. ANOVA results for Y_d .

Source	Sum of Squares	DF	Mean Square	F-Value	p -Value	Contribution (%)
Model	9.30	14	0.6640	21.51	<0.0001	
X_f	0.5273	1	0.5273	17.08	0.0010	6.78
X_s	0.0772	1	0.0772	2.50	0.1360	0.99
X_p	0.0752	1	0.0752	2.44	0.1409	0.97
X_g	0.0030	1	0.0030	0.0971	0.7599	0.04
$X_f X_s$	0.0798	1	0.0798	2.58	0.1302	1.03
$X_f X_p$	0.1583	1	0.1583	5.13	0.0399	2.04
$X_f X_g$	0.0419	1	0.0419	1.36	0.2633	0.54
$X_s X_p$	0.0006	1	0.0006	0.0189	0.8925	0.01
X_f^2	0.2259	1	0.2259	7.32	0.0171	2.90
X_g^2	2.86	1	2.86	92.57	<0.0001	36.77
$X_f X_s X_p$	0.1094	1	0.1094	3.54	0.0807	1.41
$X_f^2 X_s$	0.3076	1	0.3076	9.97	0.0070	3.95
$X_f^2 X_p$	0.4566	1	0.4566	14.79	0.0018	5.87
$X_f X_g^2$	2.16	1	2.16	69.84	<0.0001	27.77
Residual	0.4321	14	0.0309			
Lack of Fit	0.3837	12	0.0320	1.32	0.5094	not significant
Pure Error	0.0484	2	0.0242			
Cor Total	9.73	28				

The major contributor is factor X_g^2 , which contributes about 36% of the data variance with a linear effect. The second parameter is $X_f X_g^2$; its linear effect contributes about 27% of the data variance. The third factor is X_f , which contributes a percentage of 6.78%. The interaction effect between the quadratic form X_g and X_f gives a contribution of about 2.5%. This interaction effect can be inferred from Figure 11a, where the contour lines are not

linear. The interaction effect between X_f and X_p is significant, with a contribution of 3.2%, as shown by Figure 11b. The interaction effect between X_s and X_f is significant, with a contribution of 3.5%, as shown in Figure 11c.

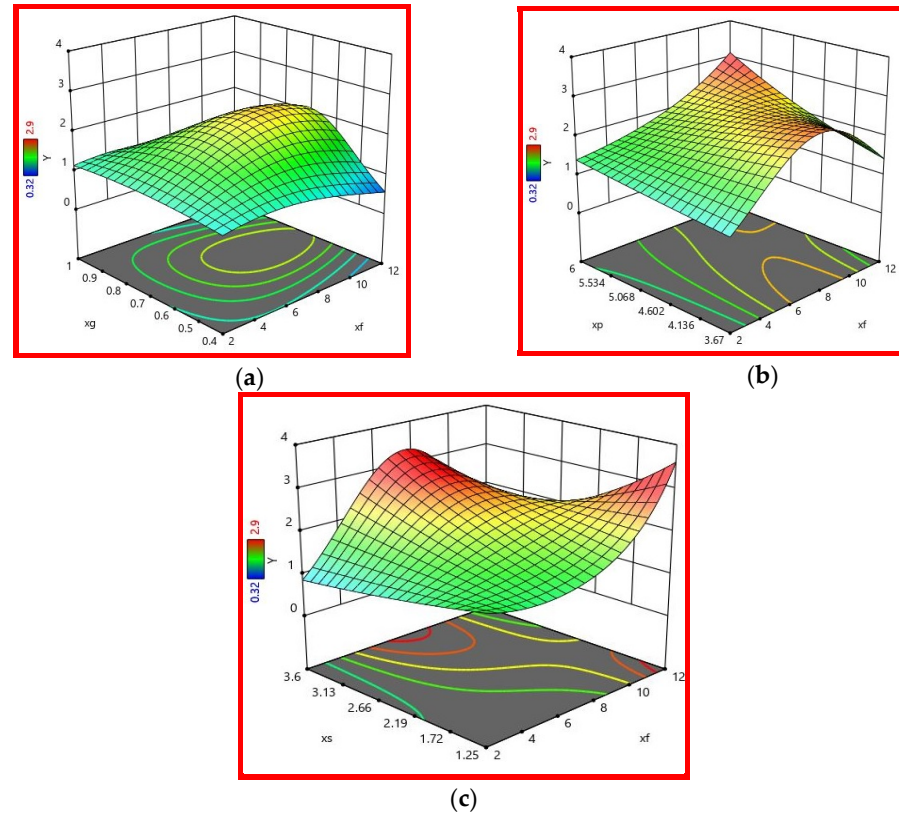


Figure 11. The interaction relationships between (a) X_f and X_g , (b) X_f and X_p and (c) X_f and X_s .

3.2.2. Regression Model for Aspect Ratio (Y_r)

The ratio can be modeled as a function of the four parameters, as is written in Equation (5) after excluding one outlier point:

$$Y_r = -0.611 + 0.1327 X_f + 0.0677 X_s + 0.0052 X_p + 2.8902 X_g - 0.012 X_f^2 X_p - 2.004 X_g^2 \quad (5)$$

The statistical indicators show the weak significance of the effects of the model's parameters on Y_r . The proposed mathematical model can be used to represent Y_r , where F-value = 6.98 and p -value = 0.0003. However, the obtained value $R^2 = 0.6556$, the adjusted value $R^2 = 0.5617$, and the signal to noise ratio $S/N = 8.094$ indicate a satisfactory fitting of the proposed equation to the data. The accuracy of the mathematical model can be represented by plotting the predicted against the experimental data, as shown in Figure 12b, and in the form of a normal plot of the residuals, as shown in Figure 12a. There is a difference in some points between the experimental and the predicted data. The ANOVA results are shown in Table 10, and these indicate the statistical significant of the equation terms. The main effect on Y_r is related to the variation in the focus point X_f . There is no interaction between the factors. The variation in Y_r is mainly related to the linear variation of X_f and the quadratic variation of X_f and X_g .

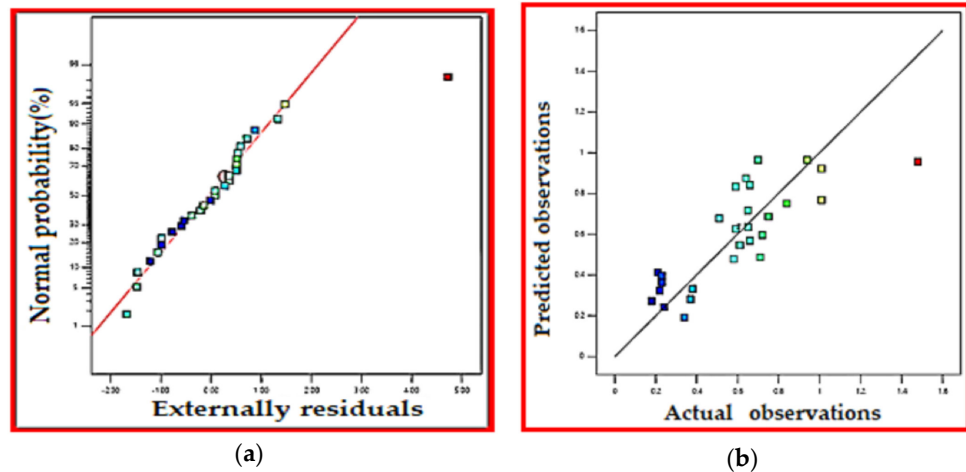


Figure 12. Model statistical indicators. (a) Normal plot of residuals. (b) The predicted observations vs. actual observations.

Table 10. ANOVA results for Y_r .

Source	Sum of Squares	df	Mean Square	F-Value	p-Value	Contribution (%)
Model	1.58	6	0.2637	6.98	0.0003	significant
X_f	0.7805	1	0.7805	20.66	0.0002	49.83
X_s	0.0469	1	0.0469	1.24	0.277	2.99
X_p	0.0006	1	0.0006	0.0157	0.9015	0.04
X_g	0.0108	1	0.0108	0.287	0.5975	0.69
X_f^2	0.235	1	0.235	6.22	0.0206	15.00
X_g^2	0.1765	1	0.1765	4.67	0.0418	11.27
Residual	0.831	22	0.0378			
Lack of Fit	0.8022	20	0.0401	2.79	0.2972	not significant
Pure Error	0.0288	2	0.0144			
Cor Total	2.41	28				

As shown in Table 10, the major contributor is the factor X_f , which contributes to almost 50% of the data variance, with a linear effect. The interaction effect between X_f and X_g can be seen in Figure 13a. It shows a contribution of 0.8%, as the contour lines are not linear. The interaction effect between X_f and X_p is not significant, with a contribution of 1%, as shown in Figure 13b.

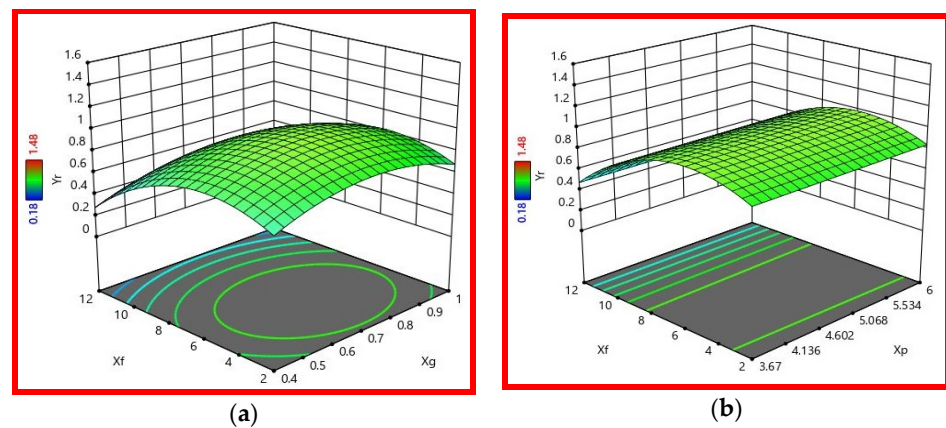


Figure 13. The interaction relationships between (a) X_f and X_g and (b) X_f and X_p .

et al. [18] stipulates that casts with a high sulfur content exhibit greater weld depth than those with low sulfur content, owing to the reverse Marangoni convection leading to deeper weld beads. On the other hand, the width of the weld bead of a low-sulfur content cast is larger than that of a high-sulfur cast, due to the occurrence of Marangoni convection.

Table 12. Percentages of occurrence of the mechanism proposed by C.R Heiple et al. [18] in the laser welding process.

Types of Weld Bead	Times Getting Partial Penetration Weld (PP) for Both Casts or Full Penetration Weld (FP) for 304 HS Cast Weld Bead out of 30 Tests	Occurrences of the Mechanism Proposed by C.R Heiple et al. [18] %	Non-Occurrences of the Mechanism Proposed by C.R Heiple et al. [18] %	Percentages of Occurrences of the Mechanism Proposed by C.R Heiple et al. [18] %
Partial penetration weld (PP) for both casts.	16	9	7	56
Full penetration weld (FP) for 304 HS and partial penetration weld (PP) for 304 LS cast weld.	14	5	9	36

In the remaining 14 cases, in which the welds were fully penetrated for 304 HS and partially penetrated for 304 LS, only in 5 tests were the mechanisms proposed by C.R Heiple et al. [18] confirmed. The role of sulfur as a surfactant is disturbed or completely reduced when keyhole-mode welding occurs. In laser welding, many complicated factors are involved, especially those associated with weld pool dynamics, melt evaporation, plasma formation, keyhole instability, the aerodynamic currents of the shield gas and the interaction between the laser beam and the plasma plume. The accumulation of hot fumes at the beam focus point, under certain conditions, can turn into a plasma cloud that strongly affects the beam, and absorbs and disperses it. All the above mentioned phenomena contribute to hiding surface active role of sulfur in determining the laser weld shape. As depicted in Table 12, the rate of achievement of reverse Marangoni convection was 56% for partially penetrated welds, compared to 36% when the welds were fully penetrated (keyhole mode). When weld penetration is governed by a keyhole mechanism, the role of surface tension gradients is diminished or completely hidden.

4. Conclusions

In this work, the effects of variations in microchemistry on the laser welding of industrial austenitic stainless steel casts 304 HS and 304 LS have been studied. The effect of laser power, welding speed, focus point position, and shield gas on depth of weld (Y_d) and aspect ratio (Y_r) were investigated using RSM. An optimal response surface design was employed to design the experiment. The model required 15 points, and another 15 points were added randomly to increase the model efficiency using Design Expert software. The following conclusions can be drawn:

- For 304 HS, the focus point (X_f) is the major factor in determining the depth of penetration of the laser weld, within a range of chosen welding parameters. The last input parameter is the main input factor, such that its contribution reaches 52.35% in determining the depth of the laser weld. The second parameter is welding speed (X_s); its linear effect contributes about 9.04% of the data variance. The third factor is the X_p , which represents a percentage of 5.66%;

- For 304 LS, the depth of the laser weld is primarily determined by the focus point, with a contribution of up to 6.78% (far greater than the other input factors if we consider only the effects of singular input factors individually). However, the interaction between shield gas and focus point distance from workpiece seems to play an important role, with a contribution of up to 28%;
- The role of the shield gas in protecting the weld pool is also linked to the level of energy supplied. Thus, at a high energy level, helium as well as mixed gas (70% He + 30% Ar) produces weld beads larger than those produced with the shield gas mixture (40% He + 60% Ar). This is attributed to the fact that helium is characterized by a high ionization potential, protecting the weld pool more effectively by expelling the plasma and ensuring less heat loss transfer. On the other hand, under a gas mixture with 60% argon, at a high linear energy, there is a risk of argon ionization causing the formation of plasma;
- A statistical study shows that a partially penetrated weld rate of 56% supports the hypothesis of the role of surface active elements in the formation of the weld pool. In contrast, in the case of full penetration welds, a rate of only 36% confirms the surface active effects of sulfur. Based on all these results, we can conclude that the laser weld morphology depends on the surface active effects of sulfur only if the chosen weld parameters result in partially penetrated welds. The surface active role of sulfur is reduced, if not eliminated, owing to melt evaporation, plasma formation, keyhole instability, the aerodynamic currents of the shield gas, and the interaction between the laser beam and the plasma. The above phenomena are more pronounced when the chosen welding parameters lead to fully penetrated welds;
- The results obtained from this work constitute an interesting database for research dedicated to the numerical simulation of thermal profiles in order to validate mathematical models. The thermal profile and solidification mode can be used to predict the microstructural and mechanical properties. On the other hand, these results may be of great use in industrial applications relating to the laser welding of thin austenitic stainless steel sheets.

Author Contributions: Conceptualization, K.T.; methodology, K.T., A.I. and R.D.; software, K.T., E.A. and A.B.; validation, K.T., E.A. and A.I.; formal analysis, K.T. and A.C.H.; investigation, K.T., R.D. and E.A.; resources, A.I.; data curation, K.T. and M.M.Z.A.; writing—original draft preparation, K.T. and E.A.; writing—review and editing, K.T., R.D. and E.A.; visualization, K.T., A.B. and A.C.H.; supervision, K.T., A.I. and M.M.Z.A. All authors have read and agreed to the published version of the manuscript.

Funding: This research received no external funding.

Data Availability Statement: The data used to support the findings of this study are included within the article.

Conflicts of Interest: The authors declare no conflict of interest.

References

1. Biswas, A.R.; Banerjee, N.; Sen, A.; Maity, S.R. Applications of laser beam welding in automotive sector—A Review. In *Advances in Additive Manufacturing and Metal Joining*; Springer: Berlin/Heidelberg, Germany, 2023; pp. 43–57.
2. Narayana, R.B.; Hema, P.; Padmanabhan, G. Experimental investigation on similar and dissimilar alloys of stainless steel joints by laser beam welding. *Adv. Mater. Process. Technol.* **2022**, *8*, 13–28.
3. Hollatz, S.; Hummel, M.; Jaklen, L.; Lipnicki, W.; Olowinsky, A.; Gillner, A. Processing of keyhole depth measurement data during laser beam micro welding. *J. Mater. Des. Appl.* **2020**, *234*, 722–731. [[CrossRef](#)]
4. Olson, D.L.; Siewert, T.A.; Liu, S.; Edwards, G.R. (Eds.) *ASM Handbook, Volume 6: Welding, Brazing, Soldering*; ASM International: Materials Park, OH, USA, 2014.
5. Kurc-Lisiecka, A.; Kciuk, M. The influence of chemical composition on structure and mechanical properties of austenitic Cr-Ni steels. *J. Achiev. Mater. Manuf. Eng.* **2013**, *61*, 210–215.

6. Dong, X.; Wang, G.; Ghaderi, M. Experimental investigation of the effect of laser parameters on the weld bead shape and temperature distribution during dissimilar laser welding of stainless steel 308 and carbon steel St 37. *Infrared Phys. Technol.* **2021**, *116*, 103774. [[CrossRef](#)]
7. Sampreeta, K.R.; Vasareddy, M.; Deepan, B.K.T. Optimization of process parameters in CO₂ laser welding of Hastelloy C-276. *Mater. Today Proc.* **2020**, *22*, 1572–1581. [[CrossRef](#)]
8. Sathiya, P.; Abdul Jaleel, M.Y.; Katherasan, D. Optimization of welding parameters for laser bead-on-plate welding using Taguchi method. *Prod. Eng.* **2010**, *4*, 465–476. [[CrossRef](#)]
9. Anawa, E.; Olabi, A.; Hashmi, M. Optimization of ferritic/austenitic laser welded components. In Proceedings of the AMPT2006 International Conference, Las Vegas, NV, USA, 30 July–3 August 2006.
10. Benyounis, K.Y.; Olabi, A.G.; Hashmi, M.S.J. Optimization the laser-welded butt joints of medium carbon steel using RSM. *J. Mater. Process. Technol.* **2005**, *164–165*, 986–989. [[CrossRef](#)]
11. Indacochea, J.E.; Olson, D.L. Relationship of Weld Metal Microstructure and Penetration to Weld Metal Oxygen Content. *J. Mater. Energy Syst.* **1983**, *5*, 139–148. [[CrossRef](#)]
12. Klapczynski, V.; Le Maux, D.; Courtois, M.; Bertrand, E.; Paillard, P. Surface tension measurements of liquid pure iron and 304L stainless steel under different gas mixtures. *J. Mol. Liq.* **2022**, *350*, 118558. [[CrossRef](#)]
13. Heiple, C.R.; Burgardt, P. Effect of SO₂ Shielding Gas Additions on GTA Weld Shape Welding. *Weld. J.* **1985**, *64*, 159–162.
14. Zhao, C.X.; Kwakernaak, C.; Pan, Y.; Richardson, I.M.; Saldi, Z.; Kenjeres, S.; Kleijn, R. The effect of oxygen on transitional Marangoni flow in laser spot welding. *Acta Mater.* **2010**, *5*, 6345–6357. [[CrossRef](#)]
15. Wenchao, K.; Zhi, Z.; Oliveira, J.P.; Bei, P.; Jiajia, S.; Caiwang, T.; Xiaoguo, S.; Wentao, Y. Heat transfer and melt flow of keyhole, transition and conduction modes in laser beam oscillating welding. *Int. J. Heat Mass Transf.* **2023**, *203*, 123821.
16. Coviello, D.; D'Angola, A.; Sorgente, D. Numerical Study on the Influence of the Plasma Properties on the Keyhole Geometry in Laser Beam Welding. *Front. Phys.* **2022**, *9*, 754672. [[CrossRef](#)]
17. Hou, Y.C.; Lu, W.; Wentao, Y. Influence of oxygen content on melt pool dynamics in metal additive manufacturing: High-fidelity modeling with experimental validation. *Acta Mater.* **2023**, *249*, 118824.
18. Heiple, C.R.; Roper, J.R.; Stagner, R.T.; Aden, R.J. Surface Active Element Effects on the Shape of GTA, Laser, and Electron Beam Welds. *Weld. J.* **1983**, *62*, 72–77.
19. Kaul, R.; Ganesh, P.; Singh, N.; Jagadeesh, R.; Bhagat, M.S.; Kumar, H.; Tiwari, P.; Vora, H.S.; Nath, A.K. Effect of active flux addition on laser welding of austenitic stainless steel. *Sci. Technol. Weld. Join.* **2007**, *12*, 127–137. [[CrossRef](#)]
20. Ding, F.; Ruihua, Z.; Nakata, K.; Tanaka, M.; Ushio, M. YAG laser welding with surface activating flux. *China Weld.* **2003**, *12*, 83–86.
21. Su, Y.; Aarts, R.G.K.M.; Meijer, J.; Guan, Q. Study on effect of active-fluxes in laser welding. In Proceedings of the International Congress of Applications of Lasers & Electro-Optics, Dearborn, MI, USA, 2–5 October 2000; Laser Institute of America: Orlando, FL, USA, 2000; pp. 35–41.
22. Kou, S. *Welding Metallurgy*; John Wiley & Sons: Toronto, ON, Canada, 1987; Volume 431, pp. 223–225.
23. Shahab, A. Contribution a l'etude de la Metallurgie du Soudage de L'inconel 625 et Des Aciers Inoxydables 304 et 316. Ph.D. Thesis, University of Nantes, Nantes, France, 1990.
24. Novák, V.; Řeháčková, L.; Váňová, P.; Sniego, M.; Matýsek, D.; Konečná, K.; Smetana, B.; Rosypalová, S.; Tkadlecková, M.; Drozdová, L.; et al. The Effect of Trace Oxygen Addition on the Interface Behavior of Low-Alloy Steel. *Materials* **2022**, *15*, 1592. [[CrossRef](#)] [[PubMed](#)]
25. Kamel, T.; Abdelil, C.H.; Rachid, D.; Abousoufiane, O.; Abdallah, B.; Albaijan, I.; Hany, S.A.; Mohamed, M.Z.A. Mechanical, Microstructure, and Corrosion Characterization of Dissimilar Austenitic 316L and Duplex 2205 Stainless-Steel, ATIG Welded Joints. *Materials* **2022**, *15*, 2470.
26. Besnea, D.; Dontu, O.; Gheorghe, G.I.; Ciobanu, R.; Cuta, A. Laser micro welding of mechatronics components, Romanian Review Precision Mechanics. *Opt. Mechatron.* **2014**, *46*, 7–10.
27. Narayana Reddy, B.; Hema, P.; Padmanabhan, G. Influence of CO₂ Laser Beam Welding Process Parameters on Mechanical Properties of Alloy AISI 4130 Steel Welded Joints. In *Recent Advances in Material Sciences; Lecture Notes on Multidisciplinary Industrial Engineering*; Springer: Singapore, 2019; pp. 65–76.

Disclaimer/Publisher's Note: The statements, opinions and data contained in all publications are solely those of the individual author(s) and contributor(s) and not of MDPI and/or the editor(s). MDPI and/or the editor(s) disclaim responsibility for any injury to people or property resulting from any ideas, methods, instructions or products referred to in the content.